Available online at www.sciencedirect.com
ScienceDirect
Trans. Nonferrous Met. Soc. China 33(2023) 3612−3624
Transactions of Nonferrous Metals Society of China
www.tnmsc.cn

Mechanical alloying and phase transition of immiscible Al/Zn system during high-pressure torsion

Chen CHEN[1,2], An-ping HUA[1,2], Jun-jie YU[1,2], Yu-lin CHEN[3], Wei-xi JI[1,2], Chen-hao QIAN[1,2]

1. Department of Mechanical Engineering, Jiangnan University, Wuxi 214122, China;
2. Jiangsu Key Laboratory of Advanced Food Manufacturing Equipment and Technology, Wuxi 214122, China;
3. School of Materials Science and Engineering, Jiangsu University, Zhenjiang 212013, China

Received 3 June 2022; accepted 6 December 2022

Abstract: Two half-disk samples of pure Al and pure Zn were mechanically alloyed via high-pressure torsion (HPT) processing, followed by post-deformation annealing (PDA). The microstructure evolution of the Al−Zn alloy was studied by scanning electron microscopy, transmission electron microscopy and molecular dynamics (MD) simulations. The results indicated that the HPT-processed Al/Zn assembly was presented as a mixture of nanocrystalline and amorphous phases. The deformation-induced special orientation of $(0001)_{Al}//(111)_{Zn}$ facilitated the interatomic diffusion, and the dislocation density reached 2.17×10^{17} m^{-2} under the pinning effect of high solid solubility. Nanocrystalline, high diffusion degree, and high local dislocation density may primarily accounted for the crystalline-to-amorphous transformation in Al−Zn alloy. Moreover, the results indicated a bimodal grain size distribution of 150−250 nm and 500−900 nm, and Zn atoms were enriched at the grain boundaries, upon subsequent PDA. Under the effect of this special heterogeneous microstructure, the prepared alloy exhibited an excellent plasticity with 160% of tensile elongation.
Key words: Al−Zn alloy; high-pressure torsion; molecular dynamics simulation; solid-state amorphization; dislocation density

1 Introduction

Severe plastic deformation (SPD) [1,2], including high-pressure torsion (HPT) [3,4], equal-channel angular pressing (ECAP) [5,6], friction stir processing (FSP) [7], and accumulative roll bonding (ARB) [8], has attracted wide attention from researchers, and the structural and multi-functional properties of the nanostructured alloys have been extensively investigated. The SPD-processed materials are capable of introducing lots of crystalline defects, dislocations, deformation twins, as well as stacking faults (SFs). The above complex features may lead to three different types of structural changes except for the grain refinement [9−11]. Firstly, steady-state intermetallic compounds are synthesized, including in-situ precipitation of Mg_2Zn_{11} and $MgZn_2$ after Mg and Zn [12] are processed by HPT and HPT-processed Al/Cu assembly, thus facilitating the formation of Al_2Cu, AlCu and Al_4Cu_9 [13]. Secondly, at room temperature (RT), two immiscible metals are used to produce a supersaturated solid solution alloy (e.g., Cu−Ta [14] and Al−Zn [15]). Thirdly, solid-state amorphization (SSA) is produced. The SSA behavior in several alloys (e.g., Al−Mg [16], Cu−Zr [17], Ti−Ni [18]) has been investigated, whereas the microscopic mechanism of SSA formation is still unclear [19]. Furthermore, the effect of SSA on the deformation mechanisms is still not clarified [20].

Corresponding author: Chen-hao QIAN, Tel: +86-13861459713, E-mail: qianch@jiangnan.edu.cn
DOI: 10.1016/S1003-6326(23)66358-7

Among various SPD processes, HPT is effective in introducing large plastic strains for grain refinement up to a steady state with the hardness and microstructure unchanged [21]. It can introduce considerable non-equilibrium grain boundaries (GBs), deformation twins, stacking faults, serious lattice distortion and other nano-structures while refining grains. Excellent mechanical properties (thermal stability and high strength) are obtained when the grain size of materials is refined to submicron/nanometer [22,23].

There have been numerous studies on Al−Zn alloys with different contents of Zn processed by HPT [24,25]. CHINH et al [26] confirmed that normal strengthening is dominant for the low Zn content. However, for high Zn contents, an unusual softening was observed due to Zn wetting of the Al GBs, such that an excellent elongation was achieved at RT (close to 150%). ALHAMIDI et al [27] studied the softening mechanism of Al−30at.%Zn supersaturated solid solution alloy after HPT for 30 turns. Their results suggested that the spinodal decomposition and the formation of equiaxed grains primarily led to softening after HPT processing. BOBRUK et al [28] performed 10 turns HPT on Al−30Zn (wt.%) alloy at different temperatures. HPT at higher temperatures produced significantly finer intragranular Zn precipitates, thus affecting the mechanical behavior that reduced the elongation to failure from 200% to only 70%. However, all of the above studies were not analyzed at atomic resolution, and the role of dislocation motion in the phase transition process was ignored. EDALATI et al [29] indicated that the Al/Al boundaries were covered by ~2.1 atomic layers of Zn atoms. Accordingly, the room-temperature grain-boundary sliding and superplasticity were achieved by engineering the Zn segregation along the Al/Al boundaries through SPD.

Recently, SONG et al [30] have found clusters with chemical short-range ordering (SRO) and dimensions of 1−3 nm in deformed supersaturated Al−Zn alloy after 10 turns HPT. The clusters with chemical SRO were different from Guinier−Preston zones, which had no clear “grain boundary” between the chemical SRO regions and their matrix. The existing research has focused on Al−Zn alloy while ignoring the mechanical alloying of pure Al and pure Zn and had never experimentally observed SSA in Al−Zn alloys via HPT. Moreover, the formation process and mechanism of the micro-structure have not been clearly explained. In this study, the mixture of pure Al and pure Zn was processed into a bulk, ultra-fine grained sample with an amorphous structure by HPT at RT. Subsequently, a PDA exhibited unusually high elongations with an amorphous crystallization. Accordingly, this study aimed to investigate the amorphous and superplastic mechanisms through MD simulation and experiments.

2 Experimental

High purity Al (99.99%) and Zn (99.99%) discs with a uniform dimension of *d*10 mm × 1 mm were cut into two halves. Subsequently, the Al discs were annealed at 839 K for 1 h, and the Zn discs were annealed at 622 K for 1 h. Two types of annealed semi-discs (Al and Zn) were placed in the HPT die (Fig. 1). The HPT processing was performed on the above samples at room temperature under the pressure of 6 GPa. The rotation started after applying pressure for 5 s and terminated after 100 turns at a speed of 1 r/min. Finally, the semi-discs were consolidated into one unity disc. The temperature rise caused by deformation was tested as less than 50 K even after 100 turns, which has little effect on the microstructural evolution. The samples processed through HPT were subsequently annealed at 473 K for 5 h to study the effect of PDA on the microstructural evolution.

The elemental distribution was examined for the processed discs by a scanning electron micro-scopy (SEM, JSM−6490LV) equipped with an energy-dispersive X-ray spectroscope (EDS, X-Max50). The phase and microstructure charac-terization was performed using a high-resolution

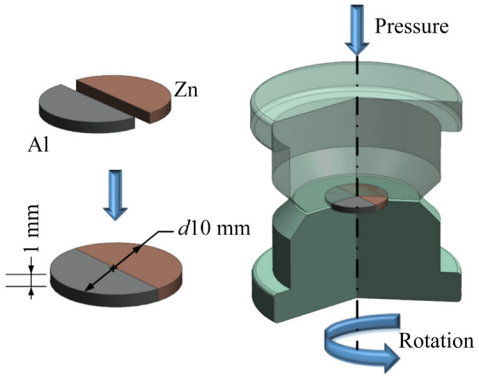

Fig. 1 Schematic illustration of HPT

transmission electron microscopy (HRTEM, JEM−2010).

All the MD simulations were performed using a large-scale atomic/molecular massively parallel simulator (LAMMPS) [31] and a modified embedded atom method (MEAM) potential for Al−Zn alloys [32]. Two initial crystalline models with the scale of 5 nm × 20 nm × 20 nm were generated as a face-centered cubic (FCC) lattice for Al, and another initial crystalline model with the size of 10 nm × 20 nm × 20 nm was generated as a hexagonal close-packed (HCP) structure for Zn, respectively. Subsequently, the initial crystalline models were merged along the x direction in the order of Al−Zn−Al, as presented in Fig. 2. The free boundary was applied along the z direction, while the periodic boundary was applied along the x and y directions. The current model structures were prepared through energy minimization. The conjugate-gradient algorithm was used for energy minimization, in which both energy and force tolerances were determined as 10^{-8}. Next, the top and bottom atoms in the above MD models were fixed as the rigid slabs, and the remaining atoms adjusted their positions at 300 K under the control of the Nose-Hoover thermostat [33,34] in the NVT ensemble. The above MD models were relaxed for 2 ns to get the most stable structures. After the optimization, the MD models were compressed with 10% of strain at first. Afterward, the constant shear velocity of 10 m/s along the x direction was applied on the top rigid slab. All visualizations in this study were performed using Ovito software [35].

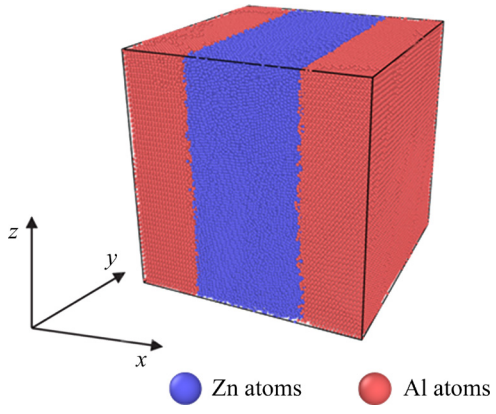

Fig. 2 Schematic view of simulation system

To verify the amorphous structure, the radial distribution function (RDF) was used to detect the distribution of Al and Zn atoms. RDF expressed by $g(r)$ is a basic function to distinguish the phase type. RDF is expressed as the average number of atoms on a sphere with a distance centered on any atom. According to different substances, the RDF is different, and the type of substance can be determined based on the change in the RDF curve. By definition, RDF is represented as [36]

$$g(r)=\frac{n(r)}{\rho_0 V}\approx\frac{n(r)}{4\pi r^2\rho_0 \mathrm{d}r} \tag{1}$$

where $n(r)$ denotes the number of atoms; V is the corresponding volume; ρ_0 represents the atomic density of the perfect crystal; r expresses the distance from the distributed atom to a given atom. Furthermore, dislocation evolution and reaction during crystallization were studied using the dislocation extraction algorithm (DXA) [37].

3 Results

3.1 Microstructure evolution

Figure 3 presents high magnification SEM images and elemental maps for Al−Zn alloy after 100 turns HPT and after 100 turns PDA. Figure 3(a) shows that some GBs were difficult to distinguish, and the elements were partially dissolved in each other according to the corresponding elemental maps (Fig. 3(b)). The structure before PDA contained three phases (Al-rich, Zn-rich, and Al−Zn mixed phases), whereas the Al and Zn grains that can be identified were nearly equiaxed grains with an average size of 100 nm. In Fig. 3(c), annealing at 473 K for 5 h induced a noticeable grain coarsening, which was inhomogeneous at grain size and the grain boundary became identifiable. The grain size of Al and Zn grains increased from 200 nm to 1 μm. As depicted in the elemental maps, the Al−Zn mixed phase disappeared, and the solubility of Al in Zn and that of Zn in Al was reduced significantly (Fig. 3(d)).

Al−Zn HPT alloy after 100 turns was further studied through TEM in Fig. 4(a). Most of the GBs were illegible and the differentiation between grains was not significant, indicating a high level of elastic distortions and atomic solid solubility in the Al−Zn HPT alloy. The grain was nearly 100 nm, consistent with SEM images. Figure 4(b) presents a HRTEM image of the intersection region of three phases, which is depicted by Zone A of Fig. 4(a). Figures 4(c−f) depict the fast Fourier transform

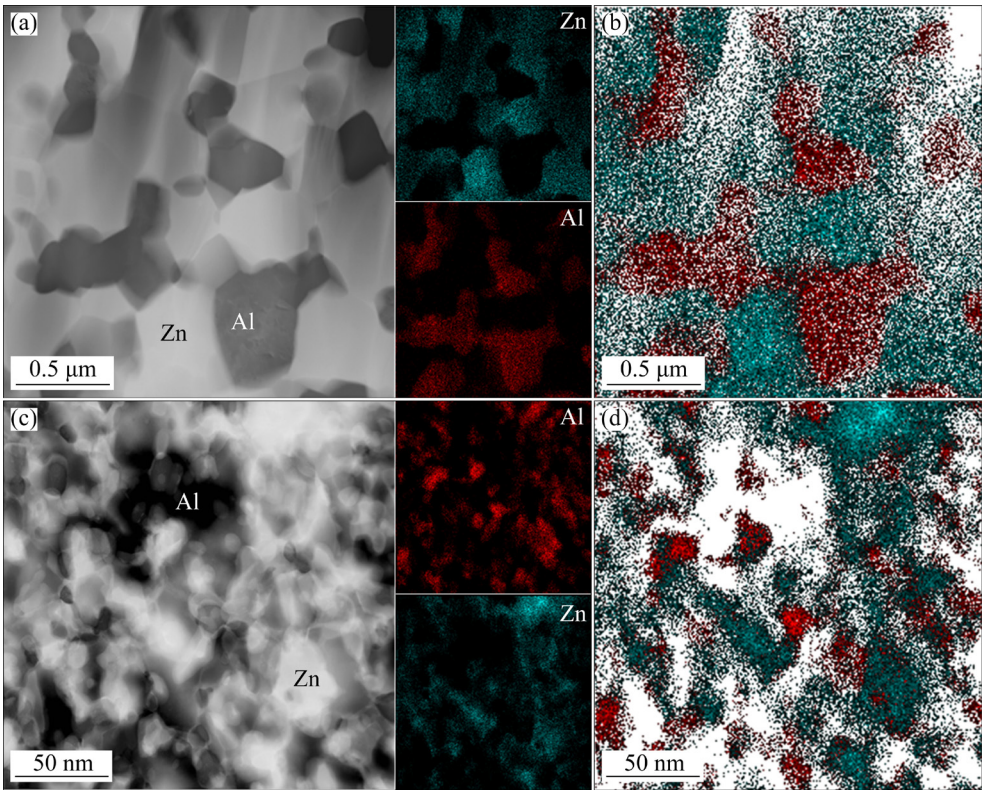

Fig. 3 SEM images of HPT sample at edge of disc: (a) SEM image before PDA with corresponding EDX map; (b) Combination of EDX maps of Al and Zn before PDA; (c) SEM image after PDA with corresponding EDX map; (d) Combination of EDX maps of Al and Zn after PDA

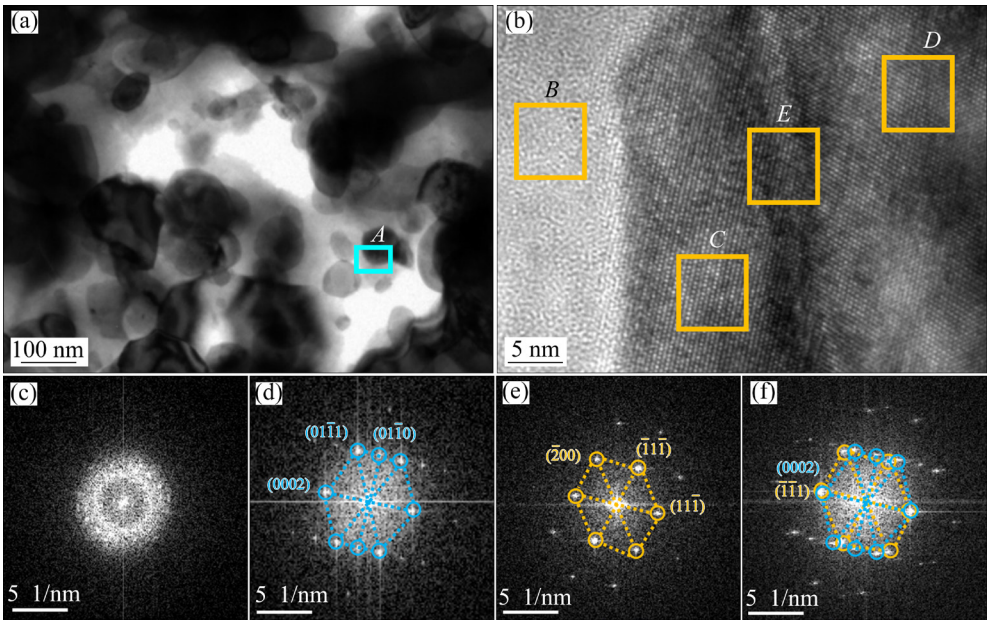

Fig. 4 TEM/STEM images of Al−Zn alloy after 100 turns: (a) TEM image; (b) HRTEM image of Zone *A*; (c) FFT of Zone *B*; (d) FFT of Zone *C*; (e) FFT of Zone *D*; (f) FFT of Zone *E*

(FFT) patterns of the corresponding zones *B*, *C*, *D* and *E* in the HRTEM image. Figure 4(c) shows a diffuse halo, confirming the amorphous structure of the Zone *A*. Figures 4(d, e) depict the significant diffraction spots corresponding to Zn and Al. By calibrating their diffraction spots, the *d*-spacing was determined as $d_{Zn}(0002)$=0.255 nm, $d_{Zn}(01\bar{1}0)$ = 0.243 nm, $d_{Al}(\bar{1}\bar{1}1)$ =0.248 nm, and $d_{Al}(\bar{2}00)$ =

0.192 nm, respectively. The calculated values were compared with the theoretical values, providing as $d_{Zn}(0002)$=0.247 nm, $d_{Zn}(01\bar{1}0)$ =0.231 nm, $d_{Al}(\bar{1}\bar{1}1)$ =0.233 nm, and $d_{Al}(\bar{2}00)$ =0.202 nm, and the comparison result indicated that the *d*-spacing changed significantly, thus suggesting high strain in lattice and an atomic inter-diffusion between Al and Zn grains. As depicted in Fig. 4(f), the diffraction spots (0002) were consistent with the diffraction spots $(\bar{1}\bar{1}1)$, thus indicating that the close-packed planes of the Zn and Al lattices were parallel to each other. Since Al and Zn have different crystalline structures, the specific orientation relationship of the close-packed planes may facilitate the atomic slip transfer, which is beneficial to enhancing the solid solubility of each other.

After annealing at 473 K for 5 h, the defect in Al−Zn alloy partially disappeared, and the grains became coarser, as shown in Figs. 5(a) and (c). It can be seen from the figures that the amorphous structure produced during HPT was crystallized into HCP structure for the Zn phase and FCC structure for the Al phase due to the sufficient annealing time. The TEM image in Fig. 5(a) shows an inhomogeneous microstructure after PDA, in which a few fine grains of 150−250 nm coexisted with primarily coarse grains of 500−800 nm in diameter. Moreover, nanoscale precipitates were clustered and showed defects primarily inside Al-rich grains. Figure 5(c) depicts a homogeneous microstructure in Zn grains presenting white grains in HAADF STEM images. In Figs. 5(b) and (d), the EDS line scan analysis across Al and Zn grains suggested that the Zn atoms, estimated as ~8 at.%, were almost uniformly distributed in Al grains, whereas the Al atoms were hardly distributed in Zn grains. Furthermore, the Zn segregation along the Al/Al grain boundary was significantly enriched compared with the inside of the Al grains. Although the EDS lines indicate that the Zn content in the interior of the GBs was nearly 20% higher than that in the grains, the actual grain boundary enrichment should be higher due to the effects of electron beam diffusion and grain boundary tilt for the electron beam.

3.2 Simulation of structure evolution

The typical time evolution of the microstructure and crystal structure fraction in HPT Al−Zn alloy is illustrated in Fig. 6. The MD model was compressed by 10% along the *z* direction during the initial 200 ps. Subsequently, a constant

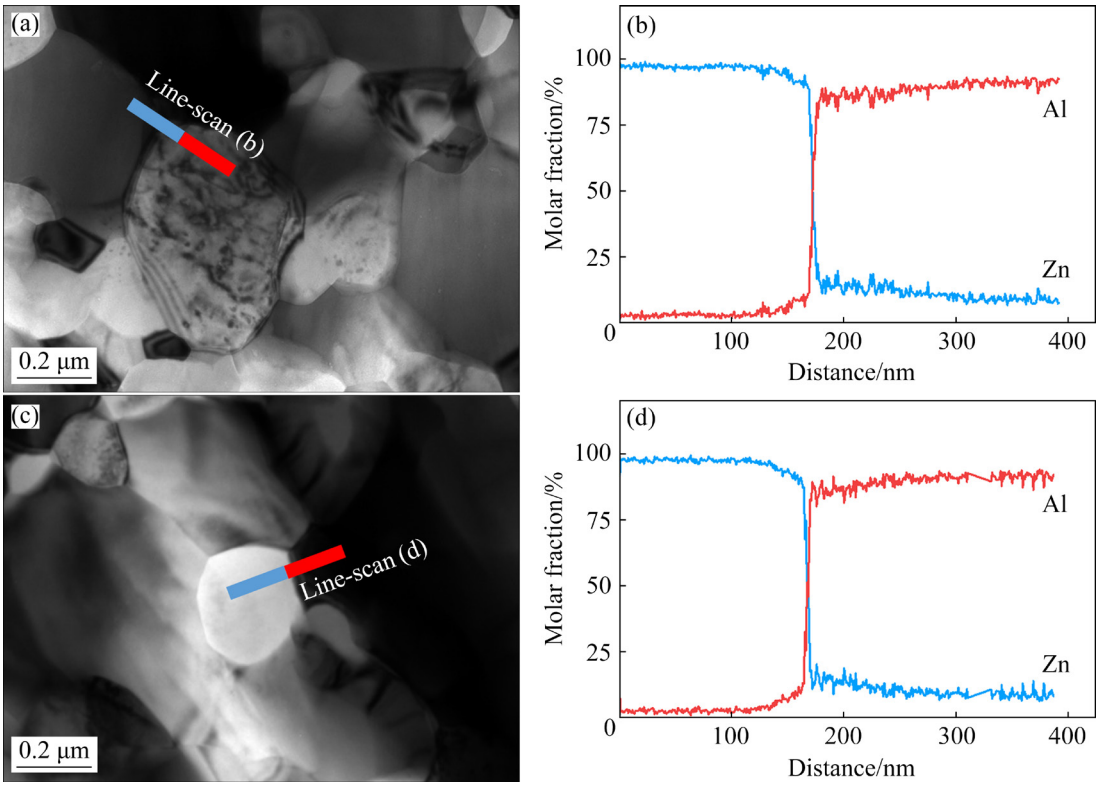

Fig. 5 TEM images and corresponding EDS results of Al−Zn alloy after PDA: (a) TEM image; (b) EDS results marked in Fig. 5(a); (c) HAADF-STEM image; (d) EDS results marked in Fig. 5(c)

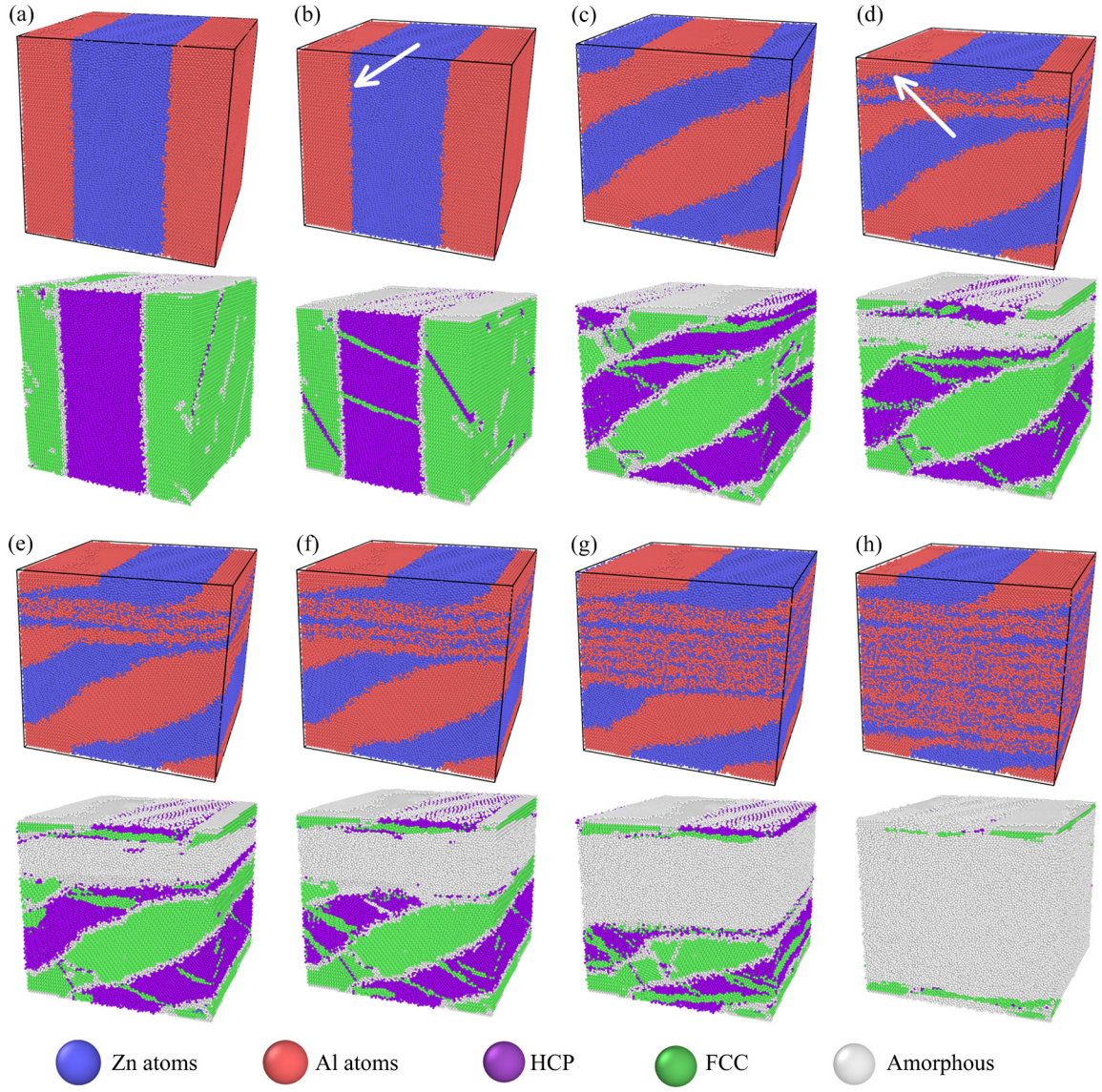

Fig. 6 Evolution of microstructure and crystal structure with time: (a) 0 ps; (b) 200 ps; (c) 500 ps; (d) 700 ps; (e) 1000 ps; (f) 1200 ps; (g) 1800 ps; (h) 2600 ps

shear velocity of 10 m/s along the x direction was applied on the top rigid slab. The grains began to stretch in the shear direction accompanied by the generation of a great number of dislocations as presented at 500 ps. As depicted in Fig. 6(c), Al and Zn grains formed a layered microstructure, and the layered microstructure was increasingly dense over time. At 500 ps, there was a significant diffusion phenomenon between Al and Zn close to the top of the model. As the atoms were moving in the shear direction, the original atoms were mismatched, and the degree of inter-atom mixing continued to increase. An amorphous structure was formed in this region according to the atom configurations in Fig. 6(d). At 700 ps, Zn and Al atoms were uniformly mixed and showed a disordered arrangement. The disordered areas that are identified (using common neighbour analysis) as the amorphous regions increased from 700 to 2600 ps. After 2600 ps, the model structure remained almost unchanged till the simulation was completed.

Figures 7(a) and (b) show the local structures of the Al−Zn phase boundaries, marked by white arrows in Figs. 6(b) and (d), respectively. At 200 ps, the matrix of Al and Zn did not show any specific orientation relationship. During the shear deformation, the crystal orientation rotated with the shear direction, thus leading to a parallel plane of (0001)Zn and (111)Al. Figure 7(c) presents the

atomic structures of the phase boundary between Al and Zn lattices. The stacking sequence in [0001] direction is ABABCABC, consistent with the results in Fig. 4(f).

Figure 8 depicts the atomic distribution of HPT Al−Zn alloy at 1800 ps. To identify the amorphous phases formed in the samples, the RDF for selected regions of the sample was calculated. The insets of

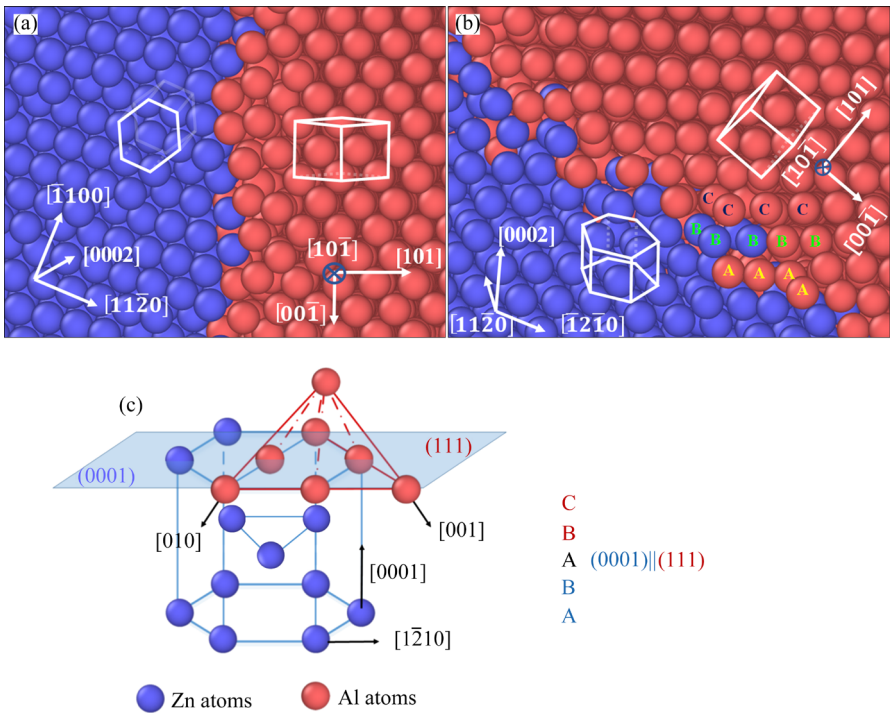

Fig. 7 (a) Structures of phase boundaries marked by white arrow in Fig. 6(b) (The matrix of Al and Zn has no specific orientation relationship); (b) Structures of phase boundaries marked by white arrow in Fig. 6(d) (The close-packed planes of Zn and Al lattices are parallel to each other); (c) Atomic structures of phase boundary between Al and Zn

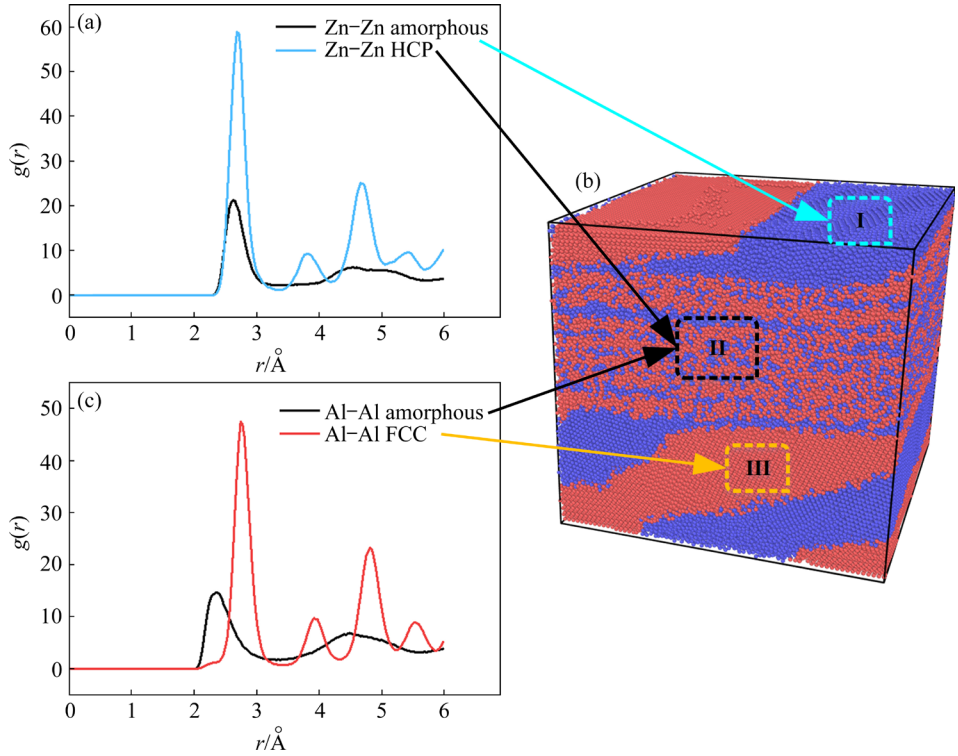

Fig. 8 RDF of specified Regions I, II and III at 1800 ps: (a) RDF of Zn−Zn in Regions I and II; (b) Crystal structure at 1800 ps; (c) RDF of Al−Al in Regions II and III

Fig. 8 present the results achieved according to Region I(top), Region II(middle), and Region III(bottom). The amorphous/crystalline structure was clearly recognized in the partial Al−Al and Zn−Zn pair RDF, with Region I corresponding to the HCP structure, Region II corresponding to amorphous phases, and Region III corresponding to the FCC structure.

4 Discussion

4.1 Amorphization by mechanical alloying

The HRTEM and MD simulation both demonstrated the SSA in the HTP-processed Al−Zn alloy after 100 turns. The mechanism of amorphization was revealed by analyzing the changing trend of dislocation density since dislocation plays a vital role in the SSA. Figure 9(a) depicts the HRTEM image of [011] zone axis in the region near the amorphization area and the corresponding FFT inset. Figures 9(b−d) present an inverse Fast Fourier Transform (IFFT) image transformed from Fig. 9(a) using the *g*-vector of $(\bar{2}00)$, $(\bar{1}1\bar{1})$ and $(\bar{1}\bar{1}1)$, respectively. As depicted in Fig. 9(b), most dislocations were 60° perfect dislocations with Burgers vectors of $1/2\langle 110\rangle$, and a considerable number of them emerged as the unidirectionally stretched dislocation loops. In fact, they were a pair of defects with opposite Burgers vectors. Besides, the red circles represent lacunal loops, and the blue circles represent vacancy loops indicating the existence of a considerable number of stacking faults and partial dislocations. In addition, the white dashed boxes mark the region with severe lattice distortion, suggesting significant internal stress in the crystal. The number of dislocations in a crystal plane was divided by the area of that crystal plane, and the dislocation density of $(\bar{2}00)$ was up to 2.1×10^{17} m^{-2}. The dislocation density on other $(\bar{1}1\bar{1})$ and $(\bar{1}\bar{1}1)$ planes was examined as 1.2×10^{17} and 9×10^{16} m^{-2}. Thus, the total dislocation density within this local area was nearly 3×10^{17} m^{-2} which is enough to directly induce SSA. Besides, the change in the crystal plane spacing of Al and Zn together with elemental maps on the SEM image after HPT suggested a high strain in lattice and a high level of atomic diffusion between Al and Zn

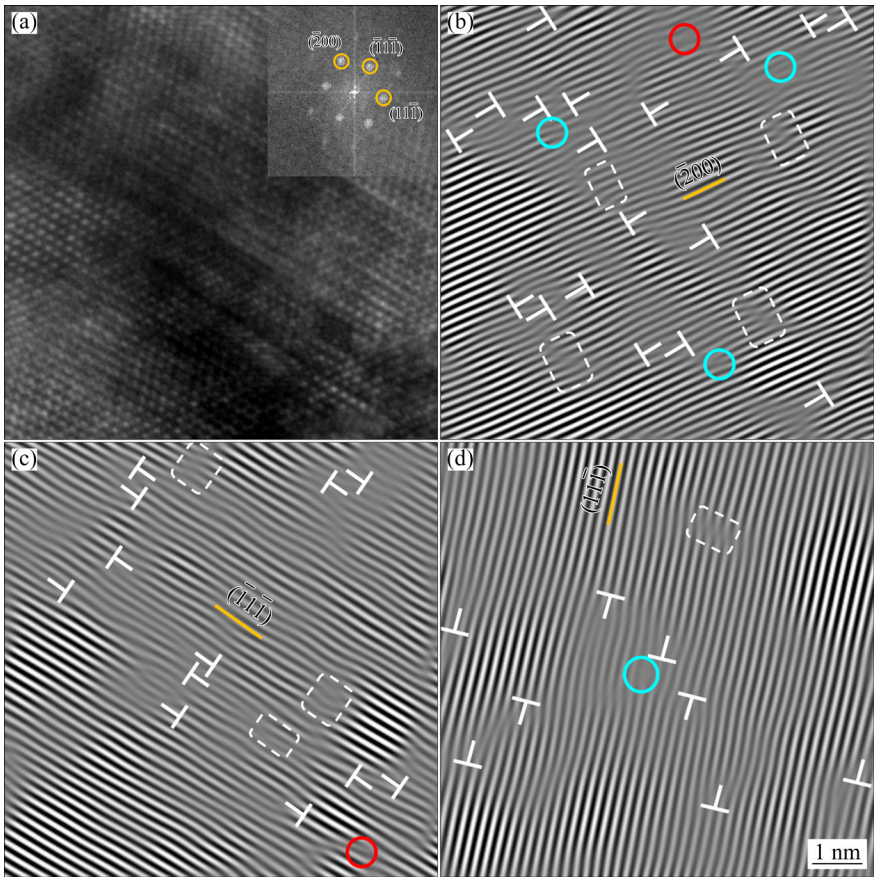

Fig. 9 [011] HRTEM image of HPT Al−Zn alloy before PDA: (a) HRTEM image of region near amorphization area grain with FFT pattern inset; (b) IFFT image of $(\bar{2}00)$; (c) IFFT image of $(\bar{1}1\bar{1})$; (d) IFFT image of $(\bar{1}\bar{1}1)$

grains. As revealed by the above analysis, severe lattice distortions and defects exist in the crystal lattice due to the high local dislocation density and atomic diffusion in the vicinity of the amorphous phase. However, in the region far from the amorphous phase, the dislocation density is relatively low, and the lattice plane *d*-spacing is close to the standard value.

Since the TEM analysis only describes the final state after the HPT processing, a MD simulation was performed to examine the transformation of dislocation and diffusion during the HPT processing. Figure 10(a) depicts crystal structure of the HPT process at 600 ps, and Fig. 10(c) presents the local regions of high dislocation density. Dislocation statistics based on DXA were analyzed on FCC of Al and HCP of Zn using different algorithms to identify the dislocations of different lattice types. The volume of the whole model was 7.07×10^{-24} m^3, and the total dislocation length was 7.71×10^{-7} m. The dislocation density of the whole MD model was calculated as 1.09×10^{17} m^{-2} as shown in Fig. 10(c). Subsequently, the local dislocation density in the area where the dislocations were concentrated was calculated to be 2.17×10^{17} m^{-2}.

Figure 11 illustrates the trend of the total and local dislocation density from 0 to 2700 ps. Notably, the microstructure evolution of MD can be divided into three stages, including the grain refinement stage, the amorphization stage, and the equilibrium stage.

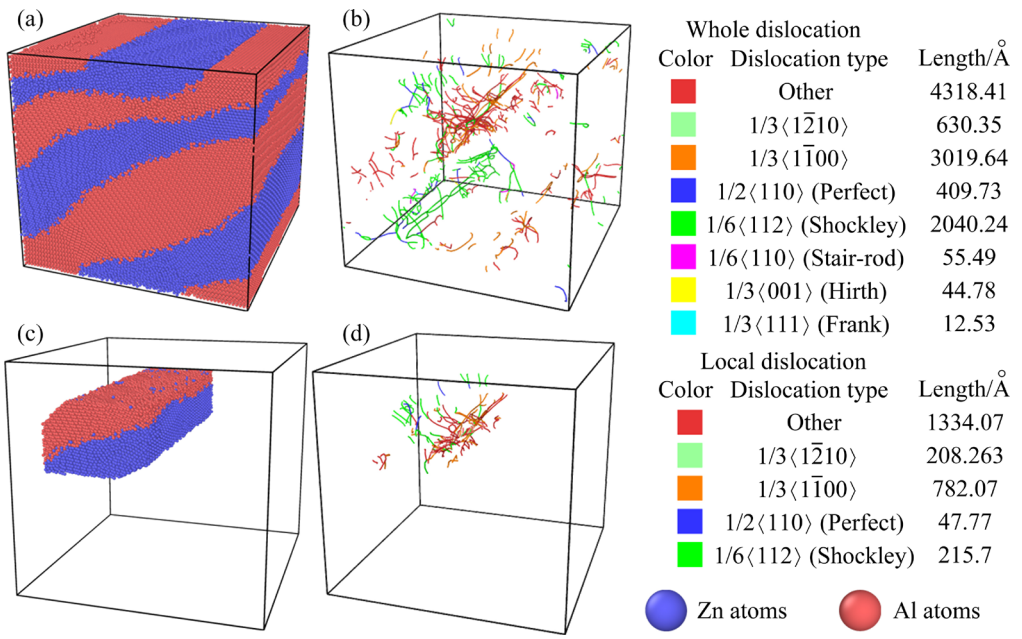

Fig. 10 Comparison of whole and local dislocation density at 600 ps: (a) Crystal structure of MD model at 600 ps; (b) Corresponding whole dislocation distribution; (c) Partial area of (a); (d) Corresponding local dislocation distribution

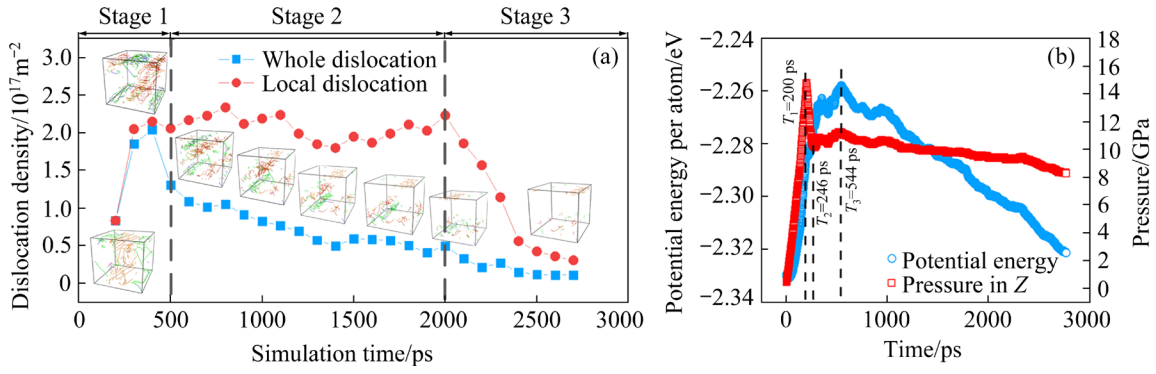

Fig. 11 Time evolution of dislocation density (a) and potential energy per atom and atomic stress (b)

At Stage 1 (grain refinement stage), with the end of the *z*-direction compression, the pressure reaches the maximum value at 200 ps, and then the shear begins. High-density dislocations were produced continuously under the action of solute and large strain. As a result, dislocation cells, SFs, subgrains, and microtwins were produced in the larger grains. Low-angle GBs of dislocation unit cells and subgrains were progressively transformed into high-angle GBs due to dislocation annihilation/stacking, dislocation interactions, as well as grain rotation and GBs slip during SPD. Thus, nanocrystalline Al−Zn alloys with high-density dislocations were formed at 400 ps.

At Stage 2 (amorphization stage), the dislocations in the nanocrystals continued to accumulate due to the solid solution of a considerable number of solute atoms and increasing strain, thus inducing a significantly high level of internal stress. The lattice instability due to elastic strain may lead to atomic mismatch, responsible for the SSA. Once SSA occurs, the dislocations in the amorphous position will disappear, so the whole dislocation density of the model will be reduced. Besides, the amorphous nucleation will contribute to the distortion of the nearby lattice. Accordingly, together with the continuous shear strain, the amorphous phase continued to expand along the nucleation area. During the above process, the whole dislocations continued to decrease, and the local dislocation density fluctuated at a higher position, as presented in Fig. 11(a). As shown in Fig. 11(b), the atomic potential energy reached the maximum at 544 ps, and then decreased with the increase of amorphous structure. Notably, amorphous disordered structure reduces the free energy of the system and the energy change is consistent with that of dislocation density.

At Stage 3 (equilibrium stage), the whole dislocation density slowly decreased to a stable value, and the local one rapidly declined. After 2400 ps, the number of dislocations remained almost unchanged, and the microstructure of the model reached equilibrium. The increase in dislocations due to continuous shear stress was balanced with the absorption of dislocation at high angle boundaries and SSA. As a result, the volume fractions of amorphous, FCC and HCP in the model were nearly unchanged.

Three conditions for the formation and growth of the amorphous phase were proposed as follows: (1) sufficient plastic deformation time for continuous generation of dislocations and other defects; (2) nanocrystalline state and local high-density dislocations within it; (3) a significant solid solubility to pin dislocations and to form high-density dislocation cells.

4.2 Characteristics of plastic deformation

It is generally known that twinning plays a major role in the plastic deformation of HCP metals. However, FCC lattice has enough slip systems to achieve good plasticity. A previous experiment suggested that the elongation of pure Zn is only about 10% [38] and about 40% for pure Al [39]. Moreover, Al−Zn alloy undergoing large plastic deformation shows a room-temperature superplasticity of nearly 150% of elongation. Some studies have found that SPD leads to the segregation of Zn precipitates at the Al−Al boundaries, which results in easy grain boundary sliding of Al−Zn alloys. Thus, superplasticity can be accomplished in Al−Zn alloys at RT. In this study, semicircle sheets of pure Al and pure Zn were mechanically mixed into a dense bulk through 100 turns of HPT. A specific orientation relationship (Fig. 4(f) and Fig. 7) was found between Al and Zn with different lattice types. The sufficient shear deformation also led to the high dissolution, thus facilitating the generation and maintenance of dislocations. Accordingly, as soon as dislocations accumulate to a certain stage, they will relax in the amorphous form. Only 15% of tensile elongation was obtained, as presented in Fig. 12, due to the brittle nature of amorphous.

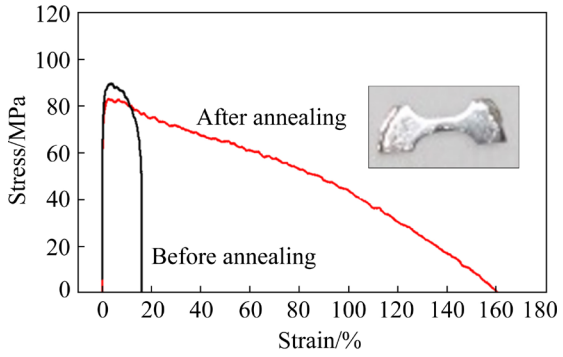

Fig. 12 Stress–strain curves obtained on HPT-processed Al−Zn samples before and after PDA

After annealing at 473 K for 5 h, the amorphous structure was decomposed into FCC Al and HCP Zn. 473 K is in the middle of the recrystallization temperature of Al and Zn (the recrystallization temperature of Al is nearly 537 and 441 K for Zn). We expect that this temperature can make Zn grains grow faster than Al grains during annealing, thus leading to the formation of a unique combination of large Zn grains + small Al grains structure. Under macroscopically uniform loading, there will be load redistribution and strain distribution in different regions (e.g., grains). The Zn grains with poor plasticity have enough deformation space for their large size, and the small-sized Al grains account for coordinated deformation. This structure is beneficial to improving the plasticity and maintaining the strength of the material. Simultaneously, Zn cluster tended to aggregate at Al−Al boundaries (Fig. 5(a)). EDS lines of Figs. 5(b) and (d) indicated that the distribution of Zn atoms at the Al/Al grain boundary was significantly higher than that within the Al grain, resulting in wetting grain boundaries. As depicted in Fig. 12, 160% super- plasticity was obtained for Al−Zn after annealing due to the initiation of the grain boundary sliding system.

While the plasticity was greatly improved, the high strength of the Al−Zn alloy remained basically unchanged. After the amorphous phase was decomposed, some zinc atoms remained in the Al grains. The pinning effect of zinc atoms on dislocation and the difference in the thermal expansion coefficient between crystalline and amorphous atoms resulted in residual dislocations in the aluminum grains. The generation of multilayered nano-lamellas was another structural feature after annealing (Fig. 13). Although the grain size increased significantly, PDA only led to a little decrease of the tensile strength from 96 to 81 MPa due to the multilayered nano-lamellas structure and residual dislocations.

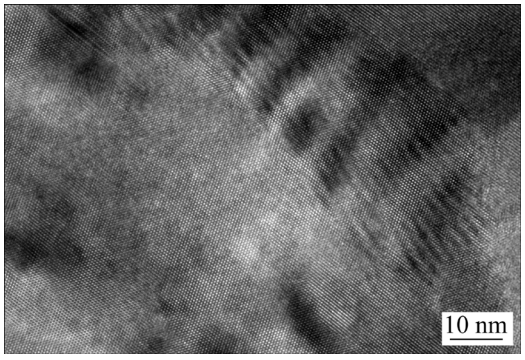

Fig. 13 HRTEM image of HPT Al−Zn alloy after PDA

5 Conclusions

(1) Mechanical alloying and phase transition occur after 100 turns of HPT deformation are applied to the two half-disk assemblies of pure Al and pure Zn which are immiscible at RT. The Al−Zn alloy after severe plastic deformation is converted into a mixture of the amorphous phase, Al nanocrystalline and Zn nanocrystalline.

(2) Specific orientation relationships based on HPT process may facilitate atomic slip transfer, thus resulting in an abnormally high atomic diffusion coefficient.

(3) The formation of SSA comprises the following stages: (1) the continuous generation of dislocations; (2) the high degree of diffusion between atoms at RT; (3) the formation of nanocrystals due to HPT process; (4) the abnormally high local dislocation density with nowhere to release.

(4) The amorphous phase nucleation promote the distortion of the nearby lattice, thus facilitating the continued expansion of the amorphous area.

(5) The PDA after 100 cycles leads to the decomposition of the amorphous phase and the formation of a heterogeneous microstructure with the Zn-rich grain boundary layer, thus facilitating the initiation of the grain boundary sliding system. The heterogeneous microstructure and grain boundary sliding system lead to a superplasticity of 160% elongation.

Acknowledgments

This work was supported by the National Natural Science Foundation of China (No. 51905215), and the Major Scientific and Technological Innovation Project of Shandong Province, China (No. 2019JZZY020111)

References

[1] BAKHSHI R, FARSHIDI M H, SAJJADI S A. Strengthening of aluminium alloy 7005 through imposition of severe plastic deformation supplemented by different ageing treatments [J]. Transactions of Nonferrous Metals Society of China, 2019, 31(10): 2909−2921.

[2] BAGHERPOUR E, PARDIS N, REIHANIAN M, EBRAHIMI R. An overview on severe plastic deformation: Research status, techniques classification, microstructure evolution, and applications [J]. The International Journal of Advanced Manufacturing Technology, 2018, 100(5/6/7/8): 1647−1694.

[3] LEVITAS V I. High-pressure phase transformations under severe plastic deformation by torsion in rotational anvils [J]. Materials Transactions, 2019, 60(7): 1294−1301.

[4] ROGACHEV S O, NIKULIN S A, KHATKEVICH V M, SUNDEEV R V, KOZLOV D A. High-pressure torsion deformation process of bronze/niobium composite [J]. Transactions of Nonferrous Metals Society of China, 2019, 29(8): 1689−1695.

[5] REN Jia-rui, SHUITCEV A V, SUN Bin, CHEN Feng, LI Li, TONG Yun-xiang. Evolution of Ti_3Ni_4 precipitates in $Ti_{49.2}Ni_{50.8}$ alloy during equal channel angular pressing [J]. Transactions of Nonferrous Metals Society of China, 2021, 31(4): 980−987.

[6] WANG Xiao-xi, ZHANG Xiang, JING Xin-yu, YUAN Jun-chi, SONG Wei. Severe plastic deformation of commercially pure aluminum using novel equal channel angular expansion extrusion with spherical cavity [J]. Transactions of Nonferrous Metals Society of China, 2020, 30(10): 2613−2624.

[7] WANG Jian, WANG Xiao-wei, LI Bo, CHEN Cheng, LU Xiao-feng. Interface repairing for AA5083/T2 copper explosive composite plate by friction stir processing [J]. Transactions of Nonferrous Metals Society of China, 2021, 31(9): 2585−2596.

[8] DU Qing-lin, LI Chang, CUI Xiao-hui, KONG C, YU Hai-liang. Fabrication of ultrafine-grained AA1060 sheets via accumulative roll bonding with subsequent cryorolling [J]. Transactions of Nonferrous Metals Society of China, 2021, 31(11): 3370−3379.

[9] SUWAS S, MONDAL S. Texture evolution in severe plastic deformation processes [J]. Materials Transactions, 2019, 60(8): 1457−1471.

[10] SEGAL V. Review: Modes and processes of severe plastic deformation (SPD) [J]. Materials (Basel), 2018, 11: 1175.

[11] KASAEIAN-NAEINI M, SEDIGHI M, HASHEMI R. Severe plastic deformation (SPD) of biodegradable magnesium alloys and composites: A review of developments and prospects [J]. Journal of Magnesium and Alloys, 2022, 10(4): 938−955.

[12] HERNÁNDEZ-ESCOBAR D, MARCUS J, HAN J K, UNOCIC R R, KAWASAKI M, BOEHLERT C J. Effect of post-deformation annealing on the microstructure and micro-mechanical behavior of Zn−Mg hybrids processed by high-pressure torsion [J]. Materials Science and Engineering A, 2020, 771: 138578.

[13] OH-ISHI K, EDALATI K, KIM H S, HONO K, HORITA Z. High-pressure torsion for enhanced atomic diffusion and promoting solid-state reactions in the aluminum–copper system [J]. Acta Materialia, 2013, 61(9): 3482−3489.

[14] MOUSAVI T, DAI J Y, BAZARNIK P, PEREIRA P H R, HUANG Yi, LEWANDOWSKA M, LANGDON T G. Fabrication and characterization of nanostructured immiscible Cu−Ta alloys processed by high-pressure torsion [J]. Journal of Alloys and Compounds, 2020, 832: 155007.

[15] YADAV D, BAURI R, CHAWAKE N. Fabrication of Al−Zn solid solution via friction stir processing [J]. Materials Characterization, 2018, 136: 221−228.

[16] CASTRO M M, SABBAGHIANRAD S, PEREIRA P H R, MAZZER E M, ISAAC A, LANGDON T G, FIGUEIREDO R B. A magnesium-aluminium composite produced by high-pressure torsion [J]. Journal of Alloys and Compounds, 2019, 804: 421−426.

[17] SUN Y F, RONG Z Y, GUAN S K. Surface solid-state amorphization of accumulative roll bonded Cu−Zr laminates by friction stir processing [J]. Materials Letters, 2020, 279: 128518.

[18] SHIMONO M, TSUCHIYA K, ONODERA H. Molecular dynamics study on amorphization of TiNi by severe plastic deformation [J]. Materials Transactions, 2013, 54(9): 1575−1579.

[19] WU X L, TAO N R, HONG Y S, LU J, LU K. Localized solid-state amorphization at grain boundaries in a nanocrystalline Al solid solution subjected to surface mechanical attrition [J]. Journal of Physics D: Applied Physics, 2005, 38(22): 4140−4143.

[20] LIU Man-ping, XIE Xue-feng, ZHANG Zhen-ya, WANG Hui, ROVEN H J. Deformation-induced solid-state amorphization in a nanostructured Al−Mg alloy processed by high pressure torsion [J]. Materials Science Forum, 2015, 817: 627−633.

[21] VORONOVA L M, CHASHCHUKHINA T I, GAPONTSEVA T M, PATSELOV A M, PILYUGIN V P, DEGTYAREV M V. Effect of single-crystal orientation on the molybdenum structure and hardness upon high pressure torsion [J]. International Journal of Refractory Metals and Hard Materials, 2022, 103: 105754.

[22] WU Sheng-hua, SOREIDE H S, CHEN Bin, BIAN Jian-jun, YANG Chong, LI Chu-nan, ZHANG Peng, CHENG Peng-ming, ZHANG Jin-yu, PENG Yong. Freezing solute atoms in nanograined aluminum alloys via high-density vacancies [J]. Nature Communications, 2022, 13(1): 3495.

[23] XU W, ZHANG B, LI X Y, LU K. Suppressing atomic diffusion with the Schwarz crystal structure in supersaturated Al−Mg alloys [J]. Science, 2021, 373(6555): 683−687.

[24] KAWASAKI M, LANGDON T G. Developing superplasticity and a deformation mechanism map for the Zn−Al eutectoid alloy processed by high-pressure torsion [J]. Materials Science and Engineering A, 2011, 528(19/20): 6140−6145.

[25] SAUVAGE X, MURASHKIN M Y, STRAUMAL B B, BOBRUK E V, VALIEV R Z. Ultrafine grained structures resulting from SPD-induced phase transformation in Al−Zn alloys [J]. Advanced Engineering Materials, 2015, 17(12): 1821−1827.

[26] CHINH N Q, SZOMMER P, GUBICZA J, EL-TAHAWY M, BOBRUK E V, MURASHKIN M Y, VALIEV R Z. Characterizing microstructural and mechanical properties of Al−Zn alloys processed by high-pressure torsion [J]. Advanced Engineering Materials, 2020, 22(1): 1900672.

[27] ALHAMIDI A, EDALATI K, HORITA Z, HIROSAWA S, MATSUDA K, TERADA D. Softening by severe plastic

deformation and hardening by annealing of aluminum−zinc alloy: Significance of elemental and spinodal decompositions [J]. Materials Science and Engineering A, 2014, 610: 17−27.
[28] BOBRUK E V, SAUVAGE X, ENIKEEV N A, VALIEV R Z. Influence of fine scale features on room temperature superplastic behaviour of an ultrafine-grained Al−30Zn alloy [J]. Materials Letters, 2019, 254: 329−331.
[29] EDALATI K, HORITA Z, VALIEV R Z. Transition from poor ductility to room-temperature superplasticity in a nanostructured aluminum alloy [J]. Scientific Reports, 2018, 8(1): 6740.
[30] SONG Z Z, NIU R M, CUI X Y, BOBRUK E V, MURASHKIN M, ENIKEEV N A, VALIEV R Z, RINGER S P, LIAO X Z. Room-temperature-deformation-induced chemical short-range ordering in a supersaturated ultrafine-grained Al−Zn alloy [J]. Scripta Materialia, 2022, 210: 114423.
[31] PLIMPTON S. Fast parallel algorithms for short-range molecular-dynamics [J]. Journal of Computational Physics, 1995, 117(1): 1−19.
[32] ZHOU X L, LI X Y, CHEN C Q. Atomistic mechanisms of fatigue in nanotwinned metals [J]. Acta Materialia, 2015, 99: 77−86.
[33] HOOVER W G. Canonical dynamics: Equilibrium phase-space distributions [J]. PHYSICAL REVIEW A, 1985, 31(3): 1695−1697.
[34] NOS'E S. A unified formulation of the constant temperature molecular dynamics methods [J]. The Journal of Chemical Physics, 1984, 81(1): 511−519.
[35] STUKOWSKI A. Visualization and analysis of atomistic simulation data with OVITO−The open visualization tool [J]. Modelling and Simulation in Materials Science and Engineering, 2010, 18(1): 015012.
[36] PEI Q X, LU C, LEE H P. Crystallization of amorphous alloy during isothermal annealing: a molecular dynamics study [J]. Journal of Physics: Condensed Matter, 2005, 17(10): 1493−1504.
[37] KUHR B, FARKAS D. Dislocation content in random high angle grain boundaries [J]. Modelling and Simulation in Materials Science and Engineering, 2019, 27(4): 045005.
[38] SRINIVASARAO B, ZHILYAEV A P, LANGDON T G, PÉREZ-PRADO M T. On the relation between the microstructure and the mechanical behavior of pure Zn processed by high pressure torsion [J]. Materials Science and Engineering A, 2013, 562: 196−202.
[39] MAVLYUTOV A M, LATYNINA T A, MURASHKIN M Y, VALIEV R Z, ORLOVA T S. Effect of annealing on the microstructure and mechanical properties of ultrafine-grained commercially pure Al [J]. Physics of the Solid State, 2017, 59(10): 1970−1977.

高压扭转过程中不混溶 Al/Zn 体系的机械合金化和相变

陈 琛[1,2]，花安平[1,2]，于俊杰[1,2]，陈昱林[3]，吉卫喜[1,2]，钱陈豪[1,2]

1. 江南大学 机械工程学院，无锡 214122；
2. 江苏省食品先进制造装备技术重点实验室，无锡 214122；
3. 江苏大学 材料科学与工程学院，镇江 212013

摘 要：通过高压扭转工艺(HPT)对两个半圆盘的纯铝和纯锌进行合金化处理以及合金化后的退火处理(PDA)。通过扫描电子显微镜、透射电子显微镜和分子动力学(MD)模拟研究 Al−Zn 合金的微观结构演变过程。结果表明，高压扭转处理的 Al/Zn 组件由纳米晶相和非晶相混合组成。变形产生的$(0001)_{Al}//(111)_{Zn}$特殊晶面取向促进了原子扩散，高固溶度的钉扎效应使位错密度达到 $2.17\times10^{17}\ m^{-2}$。Al−Zn 合金中的晶体向非晶的转变可能主要归因于纳米晶、高扩散度和高局部位错密度。此外，结果表明，退火后结构呈现 150~250 nm 和 500~900 nm 的双峰粒度分布，并且在后续的 PDA 中晶界处出现锌原子富集。这种异质微观结构使材料的伸长率达到 160%，展现出优良的塑性。

关键词：铝锌合金；高压扭转；分子动力学模拟；固态非晶化；位错密度

(Edited by Xiang-qun LI)